AIAA Scitech 2024 Forum, 8-12 January 2024, Orlando, USA, Paper number 2024-2682
DOI: 10.2514/6.2024-2682

Implicit Large Eddy Simulation of the Flow past NACA0012 Aerofoil at a Reynolds number of 1×10^5

Zhuoneng Li* and Zeeshan A. Rana†
Centre for Aeronautics, Cranfield University, Cranfield, Bedfordshire MK43 0AL, United Kingdom

In this paper, the implicit Large Eddy Simulation (iLES) incorporating an unstructured 3rd-order Weighted Essential Non-Oscillatory (WENO) reconstruction method is investigated on the flow past NACA0012 aerofoil at a Reynolds number of 1×10^5. The flow features involve laminar separation, transition to turbulent and re-attachment. Simulations are carried out in the framework of open-source package OpenFOAM with a 2nd-order Euler implicit time integration and Pressure-Implicit Splitting-Operator (PISO) algorithm is used for the pressure-velocity coupling. Conventional LES with Wall Adapting Local Eddy Viscosity (WALE) model is also carried out as a baseline. The results are compared with Direct Numerical Simulations (DNS) under the same flow configurations. The mean quantities such as pressure coefficient and the re-attached turbulent velocity profiles are in excellent agreement with the DNS reference. On the other hand, in the transitional region, the thickness of separation bubble obtained by both iLES and LES is thinner than the DNS. The current iLES approach has achieved a 35% reduction of mesh resolution compared to wall resolving LES and 70% reduction compared to DNS, while the accuracy is mostly satisfied.

I. Nomenclature

ν	=	Kinematic viscosity (m^2/s)
ω	=	Weight (-)
τ_{sgs}	=	Sub-Grid-Scale tensor
ν_{sgs}	=	SGS viscosity
$\hat{\Delta}$	=	Filter width
Re	=	Reynolds number (-)
p	=	Kinematic pressure (m^2/s^2)
$\mathbf{U}$	=	Velocity vector (m/s)
t	=	Time (s)
T^*	=	Time unit (s)
V	=	Volume of a cell (m^3)
k_{sgs}	=	SGS kinetic energy
S	=	Area of a face (m^2)
l_z	=	Span-wise extend lenth
$\mathbf{F}$	=	Surface flux (-)
$\mathbf{n}$	=	Normal unit vector of a surface
(x, y, z)	=	Cartesian coordinates (m)
x^+, y^+, z^+	=	Dimensionless distance
U	=	Free-stream velocity (m/s)
C	=	Cord length of aerofoil (m^3)
u, v, w	=	Velocity components
Q	=	Q criterion
$\mathbf{F}$	=	Flux
Ma	=	Mach number
C_l	=	Lift coefficient (-)

*Researcher, Centre for Aeronautics, Cranfield University, Cranfield, Bedfordshire MK43 0AL, United Kingdom
†Senior Lecturer in Aerodynamics, Centre for Aeronautics, Cranfield University, Cranfield, Bedfordshire MK43 0AL, United Kingdom.

C_d = Drag coefficient (-)

II. Introduction

The he most widely used Computational Fluid Dynamics (CFD) technique to simulate turbulent flows is Reynolds Average Navier-Stokes (RANS) Simulation [1–3], where a time-space averaging process is applied to the governing equations and a turbulence model is employed to account for the instantaneous quantity. Although results can be obtained quickly, the intermittent information is lost because of its statistical time-averaging concept. In more complex flow configurations such as flow past an aerofoil with moderate separation, the RANS method is not able to provide satisfactory results in capturing the flow characteristics [4–8]. Spalart and Strelets [9] have demonstrated that the turbulence models which are employed in RANS method were not designed to capture the transition accurately.

Due to the energy cascade of turbulence, Large Eddy Simulation (LES) was developed to resolve large energy-containing scales while a (Sub-Grid-Scale) SGS model is employed to account for unresolved small scales. This approach captures most of the instantaneous flow features with an acceptable computational cost compared to the Direct Numerical Simulation (DNS) approach [10, 11]. However, the complexity of construction, calibration and implementation of SGS model has limited its popularity in the wider engineering applications [12, 13]. In the context of wall bounded viscous flow, such as flow past aerofoil, the small scales in the boundary layer that are mainly responsible for transition are generally modelled by an SGS model [14], which is one of the fundamental issue to apply LES in such flow. In the context of transitional flow, the use of an SGS model in the laminar region of the flow field could introduce excessive numerical dissipation which contaminates the flow in downstream regions [15]. The investigation towards the unconventional LES approach has been encouraged because of above mentioned limitations.

Boris [16] discovered that the leading truncation error terms of the certain flux reconstruction algorithm have the similar functionality as an SGS model. An LES can be achieved without an explicit SGS model and this family of LES is generally named Implicit Large-Eddy Simulation (iLES) [13]. It should be noted that distinction should be made between iLES and LES without SGS model, as the latter is achieved by directly revoking the SGS model without a rigorous numerical analysis, where non-physical results are obtained [17, 18]. By applying Modified Equation Analysis (MEA), Drikakis and Rider[19] have showed the reconstructed convective terms of governing equations using Weighted Essentially Non-Oscollatory (WENO) scheme have the leading truncation error terms in the form similar to a SGS model, which proved the built-in SGS mechanism of WENO scheme. The WENO scheme [20] was initially developed as a shock wave capturing scheme, it has characteristic of achieving higher order accuracy in smooth regions and providing non-oscillatory solutions in highly non-linear regions, which make it particular attractive in flows involving boundary transition and separation.

The structured WENO scheme was employed as implcit LES to investigate the separated flow [21], where encouraging results were obtained regarding to its efficiency on capturing vortex dynamics and in the shear layer region. Following the work of Dumbser and Kaser[22] and Tsoutsanis et al.[23], the WENO scheme was extended to arbitrary mixed-element unstructured grids. Later, Tsoutsanis et al. [24] has further advanced the implicit LES application from inviscid flows [23] to viscous flows. More recently, Zeng et al [25] has demonstrated the capability of unstructured WENO scheme implemented in OpenFOAM [26] that satisfactory results can be obtained in the context of implicit LES for turbulent flow with fixed separation. The current research is motivated to carry out investigation on more complex flow involving boundary layer transition and separation.

The aerofoil at an angle of attack is a typical non-symmetric lifting body configuration where rich flow phenomenons are presented. The adverse pressure gradient causes the laminar boundary layer to separate from the upper surface. The vortices are gradually formed downstream of the separation location due to Kelvin-Helmholtz instability. The separated boundary layer undergoes transition to turbulent when certain conditions are met, then the boundary layer will re-attach the surface. A separation bubble is then formed and followed by a turbulent boundary layer establishment. The separation bubble on the upper side of aerofoil has a great impact on the aerodynamic characteristics [27]. Its shape and length are changing instantaneously and co-relates to the transition to turbulence and the re-attachment that determine the flow characteristics downstream [28]. In addition, unlike the attached boundary layer, the separated boundary layer can not be described by linear stability theory[29] nor by parabolised stability equations[30]. Therefore, to accurately capture the overall flow phenomena is a challenging task for the numerical methods.

The Direct Numerical Simulations (DNS) have provided valuable insights regarding to the boundary layer physics, for example, Rodriguez et al [31] addressed the mechanisms of transition of separated boundary layer of NACA0012 at full stall. Shan et al [32] explored the origin of the three dimensional instability and suggested it is linked to the interaction of vortices and wake. The benchmark data from these DNS studies provide a great opportunity to assess

current implicit LES approach. Note that Mellen et al [33] pointed out that capturing the near-wall turbulence and transition adequately is essential for a well-resolved LES. To obtain a well resolved boundary layer, the Reynolds number considered in current research is 1×10^5, which is the same as two DNS references of Shan et al [32] and Smith and Ventikos [15].

The main goal of this paper is to further evaluate the iLES capability of open-source general purpose code OpenFOAM when the application is extended from previously work (see [25]) to a more complicated flow which involves transitional and seprated boundary layer. Similarly, conventional LES with Wall Adapting Local Eddy Viscosity (WALE) [34] SGS model is also conducted as baseline. The flow past an aerofoil NACA0012 at angle of attack of 4 degrees, where a laminar separation bubble and turbulent boundary layer will occur on the upper side. It should be noted that the DNS references of Shan et al [32] and Smith [15] have predicted different results regarding the mean surface pressure coefficient, velocity profiles and re-attachment location. The current numerical simulations aims to provide additional data and address the possible cause of the discrepancy. The rest of the paper is organized as following: the detailed numerical approach including finite volume method, discretisation scheme, SGS modelling and time integration are introduced in Sec III. Next the grid, boundary and initial conditions are described in Sec IV. Then the results from the time-averaged flow are analysed in Sec V. Finally, major findings are summarised with the technical contributions in Sec VI.

III. Numerical Approach

A. The Governing Equations and Finite Volume Method

Transient three dimensional incompressible flows are described by the following Navier-Stokes equations:

$$\frac{\partial \mathbf{U}}{\partial t} = -\nabla p - \nabla \cdot (\mathbf{U}\mathbf{U}) + \nu \nabla \cdot (\nabla \mathbf{U}), \tag{1}$$

where $\mathbf{U} = (u, v, w)$ is the fluid velocity vector, ν is kinematic fluid viscosity and p is kinematic pressure obtained by static pressure divided by a constant density. The incompressibility is ensured by the continuity equation:

$$\nabla \cdot \mathbf{U} = 0 \tag{2}$$

Considering a computational point C denotes the centre of a controlled volume V_i, thus the following criterion should be satisfied:

$$\int_{V_i} (x - x_C) dV_i = 0 \tag{3}$$

where x is arbitrary coordinate inside the controlled volume V_i. In the first step of finite volume discretization process, the governing equations 1 and 2 are integrated over the finite volume cell V_i with arbitrary form, such that:

$$\underbrace{\frac{\partial \mathbf{U}}{\partial t}}_{TransientTerms} = -\int_{V_i} \underbrace{(\nabla p) dV_i}_{PressureGradient} - \int_{V_i} \underbrace{\nabla \cdot (\mathbf{U}\mathbf{U}) dV_i}_{ConvectiveTerms} + \int_{V_i} \underbrace{\nu \nabla \cdot (\nabla \mathbf{U}) dV_i}_{ViscousTerms} \tag{4}$$

$$\int_{V_i} (\nabla \cdot \mathbf{U}) dV_i = 0 \tag{5}$$

The transient terms represent the unsteadiness of flow, in the situation of steady-state, this term disappears. The pressure gradient terms account for the pressure difference of the op-positing surfaces of the controlled volume. The convective terms describe the rate of property change due to the fluid particles being transported. The viscous terms represent the rate of property change due to the viscosity of the fluid. It should be noted the body forces such as centrifugal force and gravity force are not counted in the general mathematical model of flow. The Gaussian theorem is then applied to transform the volume integrals of the convection, viscous and pressure gradient terms of momentum equations 4 into surface integrals such that:

$$\int_{V_i} \nabla \cdot (\mathbf{U}\mathbf{U}) dV_i = \int_S \mathbf{U}\mathbf{U} \cdot \mathbf{n} dS \tag{6}$$

$$\int_{V_i} \nu \nabla \cdot (\nabla \mathbf{U}) dV_i = \int_S \nu \nabla \mathbf{U} \cdot \mathbf{n} dS \tag{7}$$

$$\int_{V_i} (\nabla p) dV_i = \int_S p \cdot \mathbf{n} dS \tag{8}$$

The dS is a small fragment of the considered face of the controlled volume V_i and $\mathbf{n}$ denotes the surface normal unit vector. To evaluate the above surface integrals, a Gaussian quadrature is employed. The integral at a considered face of the cell is evaluated as:

$$\int_S \mathbf{F} \cdot \mathbf{n} dS = \sum_{g=1}^{N_g} (\mathbf{F} \cdot \mathbf{n})_{N_g} \omega_{N_g} S, \tag{9}$$

where g denotes an integration point and N_g is the total number of integration points along the surface and $\mathbf{F}$ denotes the surface flux. For a general purpose CFD code, such as OpenFOAM, one integration point located at the centre (a non-diagonal correction is often applied if centres of adjacent cells are not aligned) of the face is used with a weighting function $\omega_{N_g} = 1$, leading to a 2nd order overall accuracy in space, as it was found as a good balance between accuracy and computational cost[35]. The above surface integrals are treated as discrete ones and evaluated numerically through the use of Gaussian integration 9, such that:

$$\int_S \mathbf{U}\mathbf{U} \cdot \mathbf{n} dS = \sum_{j=1}^{N_{fi}} \mathbf{U}_{fi} (\mathbf{U}_{fi} \cdot \mathbf{S}_{fi}) = \sum_{j=1}^{N_{fi}} \mathbf{U}_{fi} \mathbf{F}_{fi}{}^0 \tag{10}$$

$$\int_S \nu \nabla \mathbf{U} \cdot \mathbf{n} dS = \sum_{j=1}^{N_{fi}} \nu (\nabla \mathbf{U})_{fi} \cdot \mathbf{S}_{fi} \tag{11}$$

$$\int_S p \cdot \mathbf{n} dS = \sum_{j=1}^{N_{fi}} p_{fi} \cdot \mathbf{S}_{fi} \tag{12}$$

where the subscript fi denotes the interpolated value on cell faces, $\mathbf{S}_{fi}$ denotes outward-pointing face area vector for the face fi, $\mathbf{F}^0$ represent the surface mass flux of current time step. Substituting Equations into 1 and performing a temporal discretisation lead to the general form of semi-discretized momentum equations:

$$\int_t^{t+\Delta t} \frac{\partial \overline{\mathbf{U}}_i}{\partial t} dt = \int_t^{t+\Delta t} \{\mathbf{RHS}\} \, dt \tag{13}$$

Where the **RHS** takes the following form:

$$\mathbf{RHS} = -\frac{1}{|V_i|} \sum_{j=1}^{N_{fi}} p_{fi} \cdot \mathbf{S}_{fi} - \frac{1}{|V_i|} \sum_{j=1}^{N_{fi}} \mathbf{U}_{fi} \mathbf{F}_{fi}{}^0 + \frac{1}{|V_i|} \sum_{j=1}^{N_{fi}} \nu (\nabla \mathbf{U})_{fi} \cdot \mathbf{S}_{fi} \tag{14}$$

And the $|V_i|$ is the volume of a finite volume cell, $\overline{\mathbf{U}}_i$ is cell averaged velocity which is evaluated as:

$$\overline{\mathbf{U}}_i = \frac{1}{|V_i|} \int_{V_i} \mathbf{U} dV, \tag{15}$$

Following the same procedure, a discretised continuity equations can be derived from 5:

$$\sum_{j=1}^{N_{fi}} \mathbf{U}_{fi} \cdot \mathbf{S}_{fi} = 0, \tag{16}$$

Currently, discretisation in both space and time is applied to original governing equations through finite volume method. In the incompressible flow, due to the absence of equation of state, an additional pressure correction needs to be constructed. The relevant detail and treatment for each term of the set of the semi-discretised equations are discussed in the following sections. Now, to solve the discretised system of equations on computer, an arrangement[36] is carried out to construct a set of algebraic equations. Thus, a linear operation is required to express the surface flux of the considered cell C by its surrounding cells N, which leads to the following form:

$$a_C \mathbf{Q}_C + \sum_{j=1}^{N} a_N \mathbf{Q}_N = \mathbf{B} \tag{17}$$

where $a_C = \sum_{j=1}^{N} a_N$ contains all the time-space discretisation information of considered cell (or target cell) C while a_N contains the time-space discretisation details of all the surrounding cells of N. The rest of information is stored in **B**. The linear procedure is then applied to all the cells of the computational domain, leading to a system of algebraic equations:

$$\begin{pmatrix} a_{C1} & a_{N2} & \cdots & a_{N_n} \\ a_{N1} & a_{C2} & \cdots & a_{N_n} \\ \vdots & \vdots & \ddots & \vdots \\ a_{N_m} & a_{N2} & \cdots & a_{C_l} \end{pmatrix} \begin{pmatrix} Q_1 \\ Q_2 \\ \vdots \\ Q_n \end{pmatrix} = \begin{pmatrix} b_1 \\ b_2 \\ \vdots \\ b_n \end{pmatrix} \tag{18}$$

$$\mathbf{MQ} = \mathbf{B} \tag{19}$$

Where **M** is the coefficient matrix (which is named "lduMatrix" class in OpenFOAM), **Q** is the solution vector and **B** is the vector of boundary conditions and source terms if they are applied. Each row of the system represents the discretised equation on the considered cell C_i. Typically in OpenFOAM, the quantics of interests such as velocity are stored in the cell centre and interpolated to cell faces linearly from the adjacent cells. Any available interpolation scheme, such as linear or upwind, TVD-scheme can be applied in the specific dictionary (fvSchemes). The **M** Matrix and the **B** vector are constructed by the user-selected schemes for every control volume of the domain and is solved iteratively by user-defined method. OpenFOAM has greatly attracted the attention from engineering and academia, not only because it can provide reliable solutions but also for the wide degree of freedoms it can offer its user for customisation. Here, it is worth to be noted that in the coefficient matrix **M**, the diagonal component a_C are coefficients of the target cell or the considered cell and off-diagonal components a_N are coefficients of the surrounding cells. A split of **M** can be conducted as:

$$[\mathbf{A} + \mathbf{H}^{'}]\mathbf{Q} = \mathbf{B} \tag{20}$$

Where **A** only contains coefficients of the considered cell a_C and $\mathbf{H}^{'}$ contains only for that of the surrounding cells a_N respectively. A further arrangement leads to:

$$\mathbf{AQ} = \mathbf{B} - \mathbf{H}^{'}\mathbf{Q} \tag{21}$$

Further simplification leads to the final form of the matrix system:

$$\mathbf{AQ} = \mathbf{H} \tag{22}$$

B. Discretisation for Convective Terms

The convective flux in OpenFOAM is computed **fvm::div(phi,U)**, where the operator **fvm::div** denotes the implicit finite volume discretisation as coefficient matrices, where a user-defined operation can be assigned. **'phi'** is a key word represents the surface flux, expressing by $\phi_{fi}(or\mathbf{F}_{fi}) = \mathbf{U_{fi}} \cdot \mathbf{S_{f_i}}$, where $\mathbf{U_{fi}}$ and $\mathbf{S_{f_i}}$ are the physical quantities interpolated at the cell face. In the following, the LUST discretisation scheme and WENO scheme will be introduced.

1. LUST Discretisation Scheme

The LUST scheme is a hybrid scheme, combining a 75% of linear scheme (central difference scheme) and 25% of linear upwind scheme [37]. As pointed out by Smith and Ventikos[15], the best performance was achieved in capturing the transitional wall-bounded flow, in their LES computation incorporated with SGS model. Besides, the same scheme is also used in the LES of Cao et al[38] and iLES of Zeng et al[25] with a satisfactory results. The linear-upwind scheme[37] is also a 2nd order scheme and it is derived from upwind scheme and returns upwind weighting factors plus a gradient-based explicit correction, as the following equation:

$$\mathbf{F}_{fi} = \mathbf{F}_C + \mathbf{L}_{Cfi}\nabla\mathbf{F}, \tag{23}$$

where $\mathbf{L}_{Cfi}$ is the length from the centre of the considered cell C to the cell face fi and $\nabla\mathbf{F}$ is calculated based on the difference of face values from 2nd-order linear interpolation, which will be discussed in the next section.

This type of approach that combines a low-order scheme and a higher-order correction term, is called the Deferred Correction approach [39]. The approach enables the use of high order schemes in the codes initially written for lower-order schemes while keeping the stability [35]. Due to the fact that difference of upwind scheme and high order schemes are added as an correction term, the convergence speed may be affected as the difference becomes larger. One technique to overcome the weakness is to introduce a limiting strategy, as described in [26]. Benefiting from Deferred Correction concept, the 3rd order WENO scheme can be incorporated in the 2nd order code.

2. WENO Reconstruction Scheme

A 3rd order WENO reconstruction is employed on the convective terms of Navier-Stokes equations, which consists of one central stencil and several sector stencils that covers all spatial directions in the vicinity of the targeted cell. The number of sector stencils is determined by the cell shape and its closeness to boundaries. Then appropriate neighbouring cells in the reference space are collected and a linear polynomial on each stencil is formulated. Finally, the WENO scheme combines the polynomials with the non-linear weights related to the smoothness of stencils.

Similarly, the WENO polynomials are applied to reconstruct the convective flux as an explicit correction, as it fits in most OpenFOAMs pressure velocity coupling algorithm. The Modified Equation Analysis[21] is conducted on the convective dominant equations, Burgers equation for instance, to provide numerical evidence that the leading truncated errors from convective terms have the same form as the SGS model.

The key steps for WENO reconstruction to convective terms of semi-discretised Equations (13) are presented here while the detailed description can be found in Martin and Ivan [26] and Pringuey [40]. Unstructured WENO scheme combines one central stencil and several sector stencils that covers all spatial directions in the vicinity of the targeted cell. The central stencil is built up by adding the neighbour cells of the targeted cell until the desired number of total cells in the stencil is reached, the construction for sector stencils follows a similar logic but with respect to the geometric condition of the cell [23]. The general form of WENO reconstruction is expressed as:

$$p_{WENO}(\xi,\eta,\zeta) = \sum_{m=0}^{N_{Si}} w_m \cdot p_m(\xi,\eta,\zeta), \tag{24}$$

$$w_m = \gamma_m \left(\sum_{m=0}^{N_{Si}} \gamma_m \right)^{-1} \qquad \text{with} \qquad \gamma_m = \frac{d_m}{(\varepsilon + IS_m)^s}. \tag{25}$$

The reconstruction is carried out in reference space (ξ, η, ζ) to eliminate the scaling effect [22] as inline within unstructured finite volume framework. The term w_m denotes the nonlinear weights which is assigned to each polynomial. The nonlinear weight is calculated according to the corresponding smoothness. d_m is the linear weight and $\varepsilon = 10^{-6}$ is a small positive number to prevent the denominator from becoming zero and $s = 4$ is the recommended exponent of the oscillation indicator, aiming to ensure that the contribution of non-smooth stencils vanishes as the cell size tends to zero. Meanwhile, IS_m is the local smoothness indicator of stencil S_m that smooth solution leads to a smaller IS_m and hence a larger weight. This property remains unchanged since[41].

The polynomial $p_m(\xi,\eta,\zeta)$ is expressed in a basis of summation of local polynomial functions $\{\phi_k\}_{k=0,\cdots,K}$ in reference space as:

$$p_m(\xi,\eta,\zeta) = \overline{\mathbf{U}}_i + \sum_{k=1}^{K} a_k^{(m)} \phi_k(\xi,\eta,\zeta), \tag{26}$$

where a_k is the degrees of freedom and the number of degrees of freedom K is related to the degree of the polynomial r by the expression:

$$K = \frac{(r+1)(r+2)(r+3)}{6} - 1. \tag{27}$$

The subscript i denotes the cell that is being constructed. To compute the degrees of freedom, a minimum of K cells are needed. In practical however, for the stability of the system, a number of 2K cells are used, as recommended by Olivier

and Van Altena [42] and Tsoutsanis et al. [24]. Since the cell-average is not affected by the transformation, it is defined in the reference space as:

$$\overline{\mathbf{U}}_i = \frac{1}{|V_i'|}\int_{V_i'} p(\xi,\eta,\zeta)\mathrm{d}\xi\mathrm{d}\eta\mathrm{d}\zeta, \tag{28}$$

where V_i' is the volume of the mapped cell of V_i. The basis functions ϕ_k must be constructed so that the conservation condition in Equation (28) is satisfied. This implies that the mean value of each basis function over V_i' is zero. With the effort of Gartner et al. [43], the memory demand and efficiency for multi-processor parallel run of the original WENO scheme code for OpenFOAM are greatly optimised to structured grid.

However, WENO can still be very expensive, as estimated in Gartner et al[43], for a computational domain consisting one million cells, a memory of 40GB is needed to store 7 matrices with 19×38 coefficients for a 3rd order WENO reconstruction. Additionally, the reconstruction is taking place at each iteration, a high overall time consuming is expected.

Similarly, the WENO polynomials (24) are applied to reconstruct the convective flux terms of (13) on one face of the cell in the reference space [26], as demonstrated in the following:

$$\begin{aligned}(\mathbf{U}_{fi}\cdot\mathbf{S}_{fi})\mathbf{U}_{fi} &= \dot{\mathbf{F}}\cdot\sum_{m=0}^{N_{Si}} w_m\cdot p_m(\xi,\eta,\zeta)\\ &= \dot{\mathbf{F}}\cdot\sum_{m=0}^{N_{Si}} w_m\cdot(\overline{\mathbf{U}}_i+\sum_{k=1}^{K} a_k^{(m)}\phi_k(\xi,\eta,\zeta))\\ &= \dot{\mathbf{F}}\cdot(\overline{\mathbf{U}}_i+\sum_{m=0}^{N_{Si}}\sum_{k=1}^{K} w_m a_k^{(m)}\cdot\phi_k(\xi,\eta,\zeta)),\end{aligned} \tag{29}$$

where the $\mathbf{S}_{fi}$ denotes outward-pointing face area vector for the face fi and $\dot{\mathbf{F}}$ denotes the surface normal flux $\mathbf{U}_{fi}\cdot\mathbf{S}_{fi}$ in reference space. Now the convective terms are approximated with an implicit linear scheme and explicit higher-order WENO scheme.

C. Time Integration

In the current research, unsteadiness is considered. To solve the time-dependent system of equations, the implicit temporal discretisation is employed. The governing equations are re-arranged that all the spatial terms are moved to the right-hand side of the equation denoted RHS:

$$\frac{\partial\overline{\mathbf{U}}_i}{\partial t} = RHS. \tag{30}$$

The system is solved by a 2nd-order time accurate backward Euler scheme:

$$\frac{\partial\overline{\mathbf{U}}_i}{\partial t} = \frac{3\overline{\mathbf{U}}_i - 4\overline{\mathbf{U}}_i^{n-1} + \overline{\mathbf{U}}_i^{n-2}}{2\Delta t}, \tag{31}$$

where n denotes the time step. Note that the order of temporal discretisation does not need to be the same as the order of spatial discretisation, the overall accuracy will be 2nd-order in this research. It should be noted, the CFL number can be larger than 1 without causing extra instability to the system, this is the primary reason that the 2nd order implicit scheme is widely used[44–46].

IV. Numercial Setup

A. Computational Domain and Grid Resolution

The computational domain extends 16 chord length (C) on the stream-wise direction and 8 chord length on the transverse direction. The current grid is designed adopted to simulations of industrial flows where hybrid unstructured grid is often employed, see Figure 1 and Figure 2. The well refined cells are clustered around the whole surface of the aerofoil to obtain a fully resolved wall and well resolved boundary layer, meanwhile, the outer region is constructed

mainly using hexahedral cells with a coarser overall resolution. Regarding the span-wise extent l_z, Zhang and Samtaney [47] has conducted a comprehensive study on a similar test case with a Reynolds number of 5×10^4 via DNS, close predictions are found for the time-averaged aerodynamic quantities and velocity field, although the leading edge separation is found notably three-dimensional with a l_z as large as 0.8C. At the same time, the DNS of Rodriguez et al [31] has recommended a $l_z = 0.2C$ is good enough to capture the largest scales of motion in full stall condition. The smallest length 0.1C is used in DNS of Shan et al [32]. Recently, the DNS and LES study is carried out by Smith and Ventikos [15], their l_z is set to 0.2C. Frohlich et al [48] has conducted highly resolved LES on separated channel flow, pointed out the span-wise length should not essentially effect the main flow features. Note the computational cost and well resolved span-wise scales of motion need to be compromised, despite the wider span-wise length may be preferable. The $l_z = 0.2C$ is therefore used in current research, the overall grid information for each reference case is summarised in Table 1.

Due to earlier-mentioned complex physics along the surface of the aerofoil, an accurate representation of the near wall

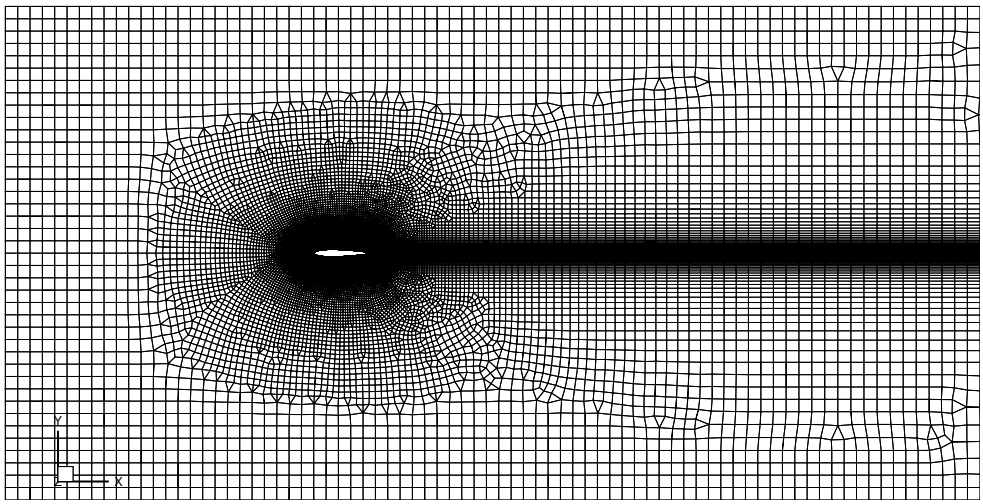

Fig. 1 Hybrid unstructured grid for NACA0012

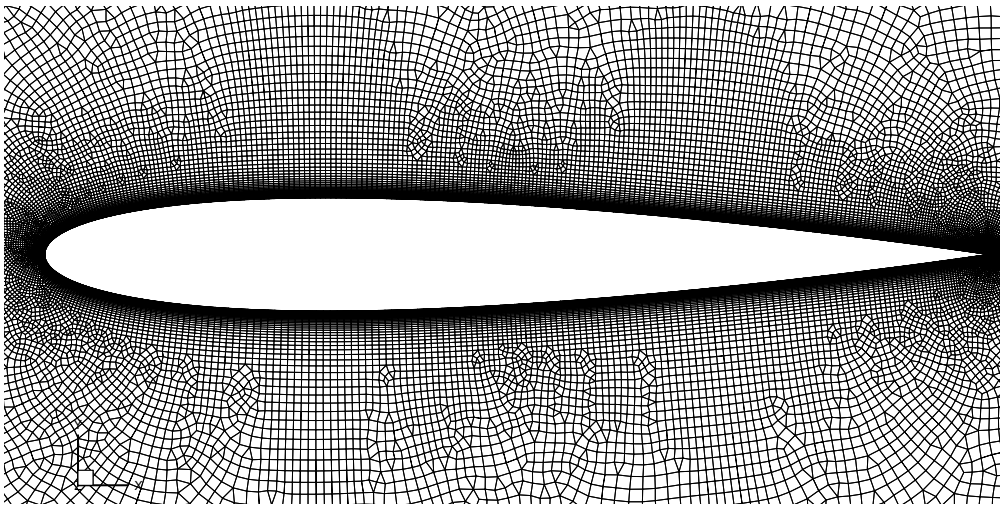

Fig. 2 Zoom view of the grid

structures is essential, therefore a well refined grid at the wall must be adopted. Here, the first cell height Δy is set to be 0.00012C with an expansion rate of 1.1 for the following cells in the wall normal direction, 150 cells are equally

Case	Re	Ma	AOA	Total	z	Lz
Shan et al [32]	10^5	0.2	4	6.9×10^6	180	0.1
Rodriguez et al [31]	5×10^4	-	12	49×10^6	-	0.2
Zhang [47]	5×10^4	-	5	134×10^6	256	0.8
Smith and Ventikos Grid D [15]	10^5	0.015	4	25×10^6	-	0.2
Current	10^5	0.1	4	7.7×10^6	150	0.2

Table 1 Global grid resolutions of previous DNS studies

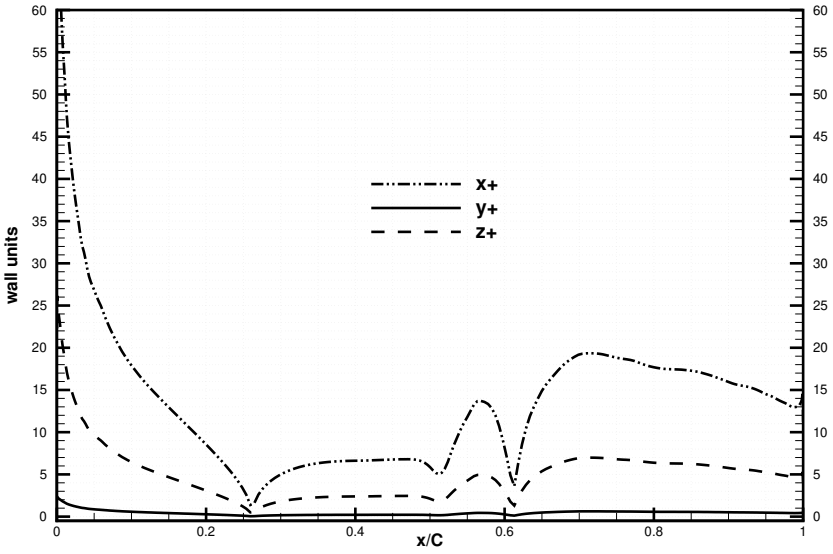

Fig. 3 Wall resolutions

distributed in the span-wise direction, gives an averaged $\Delta z = 0.0013C$. The averaged cell length in the stream-wise direction $\Delta x_{avg} = 0.0036C$, where the minimum value is $0.0005C$ at leading edge and trailing edge. The computed values for x^+, y^+ and z^+ along the upper surface of the aerofoil are plotted in Figure 3. Apart from a tiny portion of y^+ is slightly higher 1 at near the leading edge, the overall value is remained under 0.9 and approximately equals to 0.5 in the separation region, the slightly exceed y^+ value is not affect the results [15]. The average x^+ value is less than 20 for most of the area and z^+ is below 9, current wall resolutions are comparable to wall resolved LES of Asada and Kawai [45]. Piomelli and Balaras [49] and Piomelli [50] discussed extensively the grid requirements for wall resolved LES, they estimated that grid resolution at the wall should be in the range of $50 \backsim 150$ in stream-wise direction, less than 2 in wall normal direction and $15 \backsim 40$ in span-wise direction. The current wall resolutions should be considered sufficiently fine, these parameters are displayed in Table 2 with high fidelity references. It is also worth mention that the total number of cells is far less than that of DNS references [15, 31, 47] since the current numerical framework (LES) is not to fully resolve all the scales of motion of the field, the grid cells are much coarser in the laminar region away from the aerofoil surface.

B. Boundary Conditions and Flow Initialisation

The free stream Mach number 0.1 corresponds to a velocity magnitude $|\mathbf{U}|_\infty$ of 34.3m/s. The aerofoil is inclined at 4 degree, resulting a velocity vector of $\mathbf{U} = (34.2, 2.4, 0)$. A fixed inlet boundary condition is imposed at inlet and convective boundary condition is applied at outlet. The non-slip condition is applied at the aerofoil surface. The Neumann condition (zero pressure gradient) is used for pressure at inlet and the aerofoil surface, while at outlet, the

Case	x^+	y^+	z^+	Δt^*
DNS of Shan et al [32]	13	1	15	$8.35 * 10^{-5} c/U$
DNS of Rodriguez et al [31]	7	0.8	3	-
DNS of Zhang [47]	5.6	0.9	10.8	$2.5 * 10^{-4} c/U$
DNS of Smith and Ventikos Grid D [15]	8	0.6	8	$3.33 * 10^{-4} c/U$
LES of Asada and Kawai [45]	25	0.8	13	-
Current	20	0.8	10	$3.43 * 10^{-4} c/U$

Table 2 Wall resolutions and time step compare with high fidelity references

Cases	Duration (T*)	Total CPU Time (h)	Execution Time/Iteration (s)
LES	24	1214	4
iLES	24	2280	7
DNS case D[15]	30	50000	-

Table 3 Computational time

pressure value is fixed at 0. Finally, the periodic boundary condition is applied for faces in the span-wise direction. A steady-state RANS simulation with Spalart-Allmaras turbulence model is ran for 500 iteration to get a more converged initial field, as it also helps reducing the time needed to obtain statistically converged results for later analysis [15]. From the initialised field, LES is ran for a period of $TU/C = 24$ time units T^*, corresponding a physical time of 0.7s. The time step Δt of 1×10^{-5}s is defined to obtained a CFL number less than 1.5. A total iteration of 70 000 is needed for $24T^*$, the data is collected and averaged for the last $12T^*$ after the initial transient period. The statically convergence is reached after $10T^*$.

V. Analysis and Discussion

A. Computational Cost

The details regarding computational cost is summarised in the following Table 3. A total number of 128 CPUs were used for each simulation, which is half of that in DNS case D [15]. The amount of CPU hours required to carry out necessary simulation steps are significantly less for current iLES and LES, however, the iLES based on 3rd order WENO scheme is almost twice more expensive than LES based on WALE SGS model. It should be noted, approximately 3100 seconds were allocated to the calculation of the smooth indicator matrix for WENO scheme and in addition to general storage, 3rd WENO scheme requires an extra 400G for storing matrix coefficients in order to accelerate the reconstruction process [43]. Thus 3rd order WENO based iLES is generally more expensive than WALE based conventional LES.

B. Lift and Drag Coefficients

The basic aerodynamic characteristics are immediately reflected by the mean lift and drag coefficients. The lift and drag coefficients obtained by iLES and LES approaches are plotted in function of simulation time in the following Figure 4. At the early stage, the force coefficients are significantly affected by numerical transients. After dimensionless time T^*=5, the coefficients tend to be stabilised, with C_l a mean value around 0.5 and C_d is about 0.02. Note the DNS studies [15, 32] of same flow configuration (Reynolds number 100 000, AOA=4) didn't provide the force coefficients. For reference, the data from experiment of Sheldahl and Klimas [51] at Reynolds number of 80 000 are extracted, the red line represents the mean value at AOA=4 degrees and green line represents AOA=5 degrees respectively. It can be concluded that the mean forces coefficients obtained by current iLES and LES are statically converged after dimensionless time T^*=12 with barely distinguishable values, in addition, they are in reasonable agreement with reference data.

C. Mean Pressure Distribution and Skin Friction along the Surface

The distribution of mean pressure coefficient along the aerofoil surface is displayed in Figure 5, including the DNS data of Shan et al [32] and Smith and Ventikos [15]. From the leading edge to approximately x/C=0.2, the pressure is gradually increasing towards the downstream direction, generating adverse pressure gradient (∂p/∂x>0) which causes

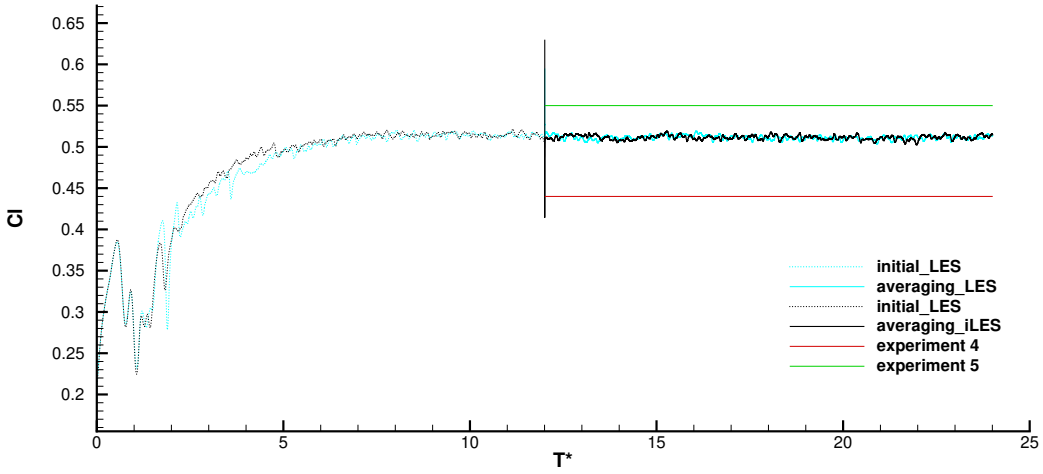

(a) Lift coefficient

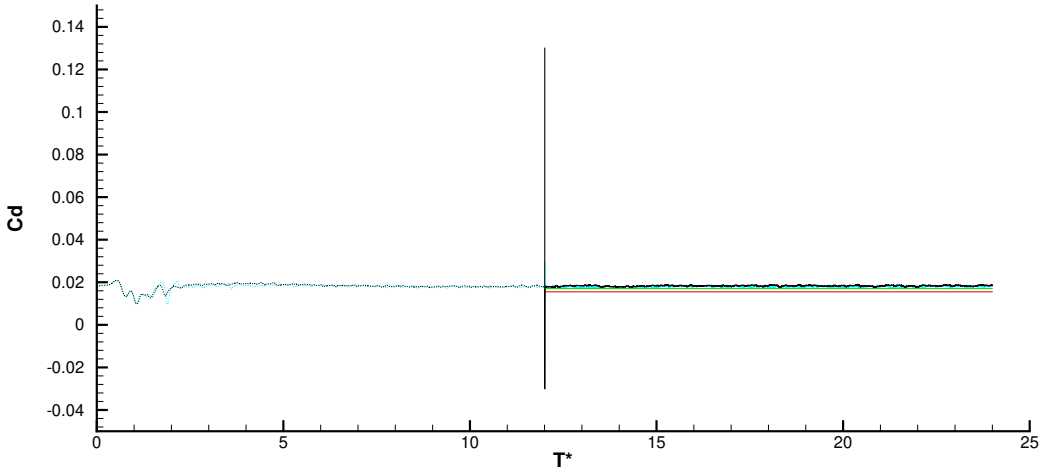

(b) Drag coefficient

Fig. 4 Force coefficients compared with experiment data of Sheldahl and Klimas [51] at AOA=4 degrees (red line) and 5 degrees (green line) degrees

the boundary layer to separate from the upper surface. A flattened plateau (0.3<x/C<0.53) denotes the laminar region of the separation zone, followed by a stronger second adverse pressure gradient ($\partial p/\partial x>>0$), where the separated boundary layer undergoes transition to turbulence(0.53<x/C<0.6). The current observations are found similar to the flat plate case [9, 52] and consistent with other LES investigations on aerofoil [53–55]. A noticeable variation of mean values which are obtained by different averaging period (T^*) can be observed in the laminar separation zone (0.2<x/C<0.65), it reveals that the size of separation bubble is related to simulation time. Overall, the mean pressure coefficients (T^*=24) from current iLES and LES are in good agreement with DNS of Smith [15] while in the transitional and turbulent region (0.55<x/C<0.65), the iLES predicted a more consistent pressure distribution. However, evident disagreement is found when comparing to DNS of Shan et al [32], the pressure is increasing faster downstream of the leading edge, a much greater "bump" appeared in the transition zone then an under-predicted pressure was predicted near the trailing edge zone.

The skin friction is often assessed in precious studies as an indicator of flow status, such as a vanishing wall shear stress is the result of flow separation. The current mean values are plotted in Figure 6 and compared with DNS results of Shan et al [32]. The mean separation zone is estimated by zero crossings of mean skin friction coefficient with a length of 0.36C, where the mean separation location and mean re-attachment locations are lying approximately at x=0.24C and x=0.60C respectively. The current re-attachment location for LES and iLES is very cloes to that of DNS of Smith [15] who predicted a mean re-attachment at x=0.56C, however, according to the DNS results of Shan et al [32], the flow re-attached at a further downstream location x=0.68C and a much longer separation bubble with a length of 0.49C was obtained. It was pointed out that size of separation bubble is related to time because of the large-scale oscillations in the three-dimensionality flow [32]. Note current simulations were ran for a duration of 24 time units and 30 time units for both Smith [15] and Shan et al [32], thus the reason for the disagreement should exclude the time convergence. It is worth mentioning that the negative skin coefficients in the plots indicating the boundary layer separation and should always remain negative until the re-attachment further downstream.

At around x=0.5C, a slightly recovery followed by a negative surge immediately occurs, indicating the onset of transition which agrees qualitatively with Spalart and Strelets [9] and Alam and Sandham [52]. On the other hand, a recovery to positive values was obtained by Shan et al [32] in the middle of separation zone, due to an additional thin layer of the mean flow near the wall in the stream-wise direction under the reversed flow. The accurate representation of boundary layer development is therefore in doubt as this thin layer was not observed in various other high fidelity simulations neither [15, 28, 53, 55, 56]. At location x=0.58C, a negative peak was reached by current simulations, then recovered towards positive value rapidly, indicating the end of laminar transition to turbulent boundary layer. After the re-attachment at x=0.6C, the skin friction coefficient continues to increase to a higher positive value quickly then gradually drops down. The DNS of Shan et al [32] have shown a similar trend, apart from largely delayed transition, re-attachment and an "oscillated" post-attachment. On the lower surface, the computed skin friction coefficients are non-distinguishable for current iLES and LES, additionally, the flow remains laminar and attached for the most of the cord length. The separation occurs at the location near the trailing edge, which will be explored in later section.

D. Mean Velocity, Turbulent Stress Profiles and Flow Field

The time averaged stream-wise velocity field and its fluctuation field in the mid-span are illustrated in Figure 7a and 7b respectively, both fields are obtained by iLES approach. At the leading edge, a small separation zone can be observed. As the fluid particle hits at the solid wall, it bounces backwards then being pushed by the following stream-wise particle, thus naturally forming a small re-circling flow zone at the leading edge area. Downstream of the leading edge, a long and thin region with considerable reversed flow is formed due to separation and re-attachment of the boundary layer which are located approximately at x=0.2C and x=0.6C, respectively, where the skin friction coefficients are zero, as seen in 6. The thickness of the separation bubble is gradually increasing and reaching its maxima at around 75% of total bubble length. The mean stream-wise fluctuation remains low and isotropic in the attached laminar region and most part of the separated region, then it increases quickly where the separation bubble becomes thickest and the peak value is clustered around the re-attachment location of the boundary layer. After the re-attachment, the mean stream-wise velocity in the near wall region (y<0.05C) has recovered a magnitude of 50% of the free-stream and stays attached until sweeping off the aerofoil surface into the wake. Meanwhile, the mean fluctuation is gradually decreasing but remains at a greater magnitude than that of attached region. On the lower surface of the aerofoil, the flow is always attached, apart from a smaller reversed flow region at near the trailing edge, corresponding the zero crossing of skin friction coefficient

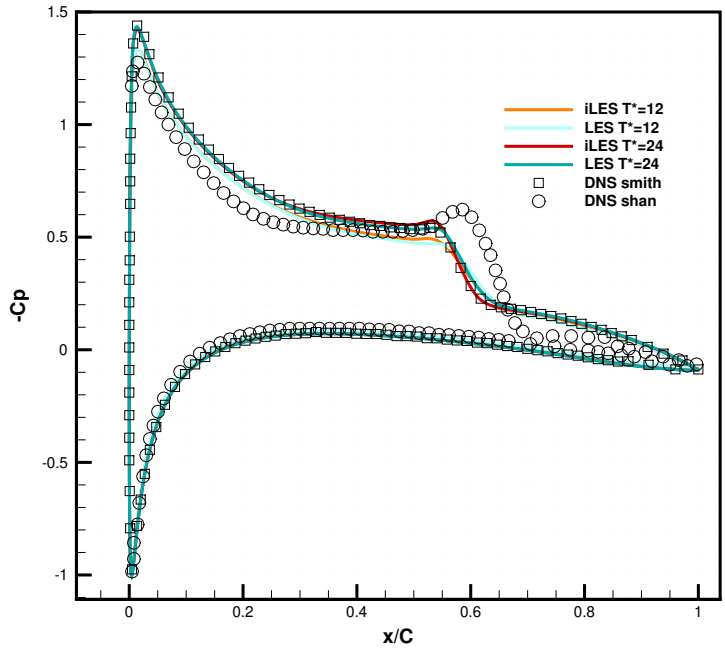

Fig. 5 Mean pressure coefficient, T^*=12 denotes the dimensionless time when vortex shedding is stabilised

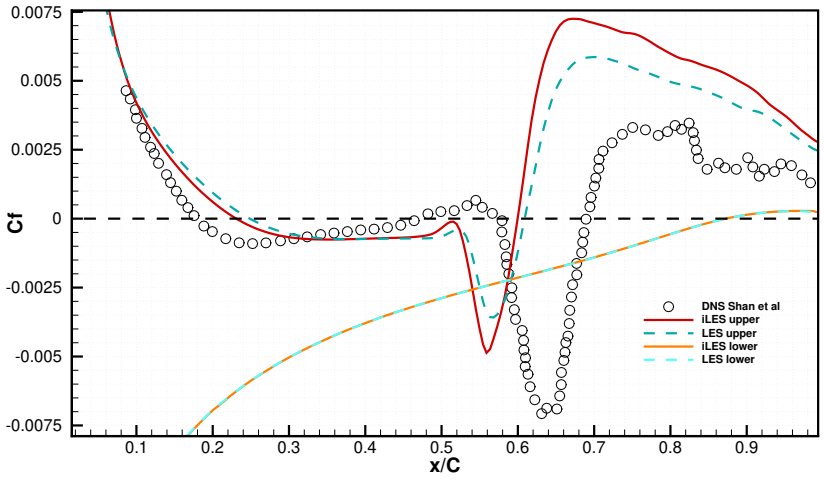

Fig. 6 Mean skin friction coefficients, note the sign of values on the lower surface are intentionally reversed

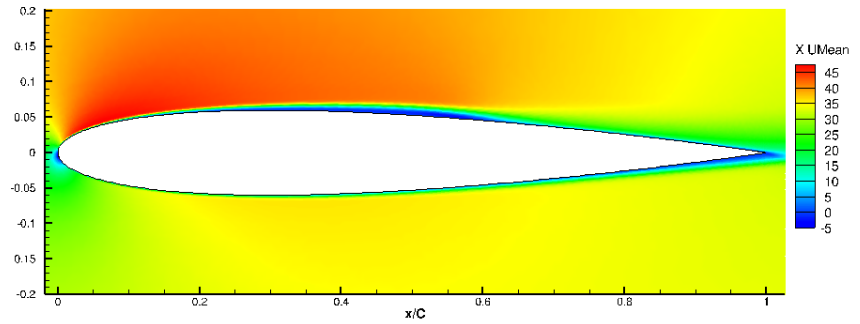

(a) Mean stream-wise velocity field

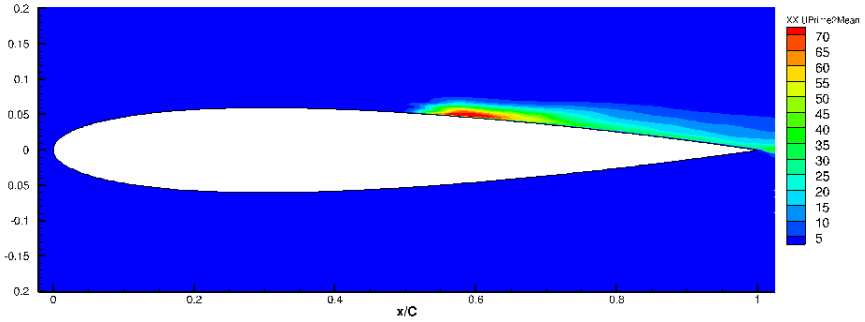

(b) RMS mean stream-wise fluctuation field

Fig. 7 Time-averaged velocity field, obtained by iLES

in Figure 6.

Figure 8 shows the enlarged view of mean separation region and is demonstrated by time-averaged velocity vectors field. One can observe that the mean separation is located around x=0.23C where the inflection point close to the wall is found. The reversed flow becomes stronger gradually downstream of the separation bubble. A second inflection point appears at around x=0.6C, indicating the re-attachment of the boundary layer. Note that at the location 0.05C upstream of the re-attachment, the reversed flow is the strongest then quickly compromised. After the re-attachment, the mean velocity field is established within a short distance and the magnitude is amplified compare to post separation. It should be noted the mean velocity vector plot of Shan et al [32] shows an additional thin layer underneath the reversed mean flow and this thin layer forms approximately 22% of total separation region. It is worth mention that their predicted mean separation length is 0.5C which is 0.14C longer than that of current and similar to the length of that additional thin layer. As shows in Figure 5, the mean separation and re-attachment predicted by current simulation is supported by recent DNS of Smith [15]. The disagreement could be allocated to the insufficient span-wise extent to accommodate major scales of motion in span direction since an extent of 0.1C was used in Shan et al [32] while at least 0.2C was employed in other similar DNS studies [15, 31, 47] where no such additional layer was identified.

To further validate current numerical method and gain more details on the averaged field, mean velocity profiles and root mean squared fluctuations are extracted at consecutive locations with an interval of 0.1C from the leading edge to the tailing edge of the aerofoil.

Figure 9 shows mean stream-wise velocity profiles, the vertical distance from the wall is converted to dimensionless form to keep consistent with two main DNS references [15, 32]. Comparing to DNS of Smith [15] (figure on the left), discrepancies are found obviously at locations from x=0.2C to x=0.6C, corresponding to the separation zone. Since the wall is considered resolved, the disagreement with DNS are mainly outside the viscous layer ($y^+ > 10$) for both iLES and LES approaches, therefore a better grid refinement to cover the entire separation zone seems to be necessary. It should be noted that the current expansion ratio of wall normal grid is set to 1.1, which could be considerably reduced to a smaller value. Despite of this, the fully turbulent velocity profiles post re-attachment at locations x=0.7C, 0.8C, 0.9C and 1C are in excellent agreement with the DNS [15]. It's worth pointing out that at re-attachment location x=0.6C, the profile given by LES approach is in better agreement that iLES. Comparing to DNS of Shan et al [32] (figure on the right), a good agreement is found at locations x=0.2C and x=0.3C, where the boundary is just separating from the

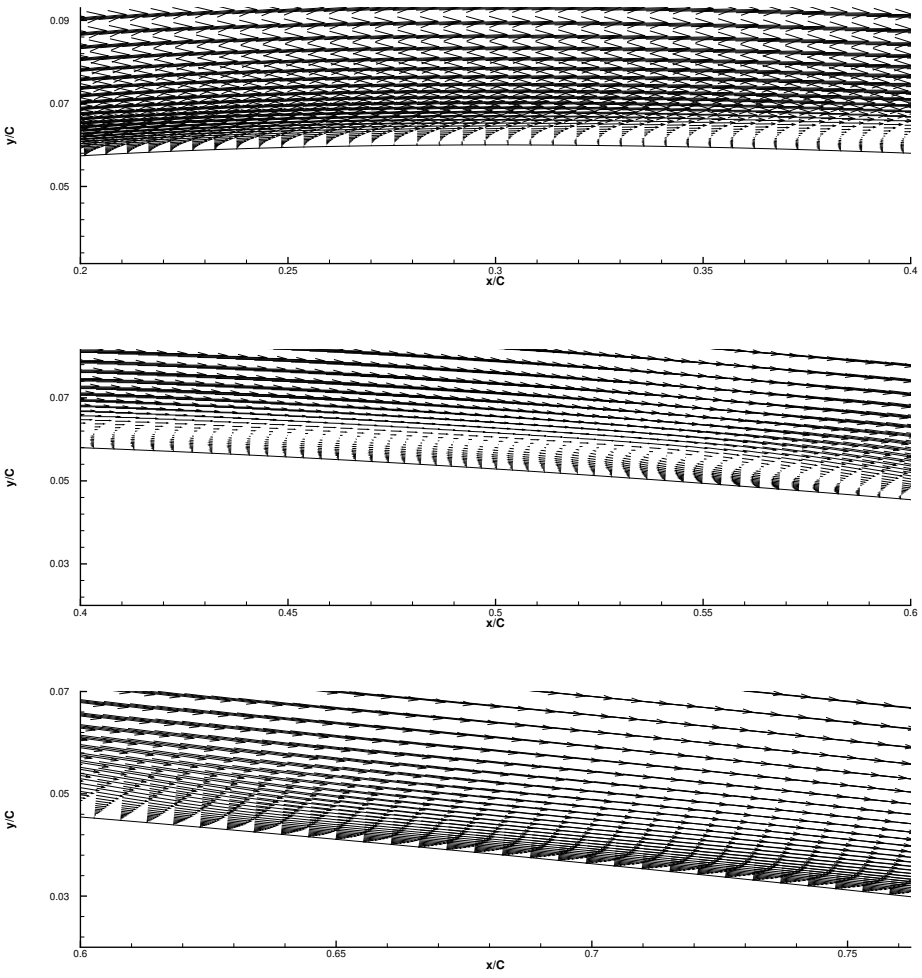

Fig. 8 Primary separation bubble on the upper surface obtained by iLES. The bubble consists of three regions: the top shows the laminar separation region, the middle shows the transitional region, the bot shows the turbulent re-attachment region

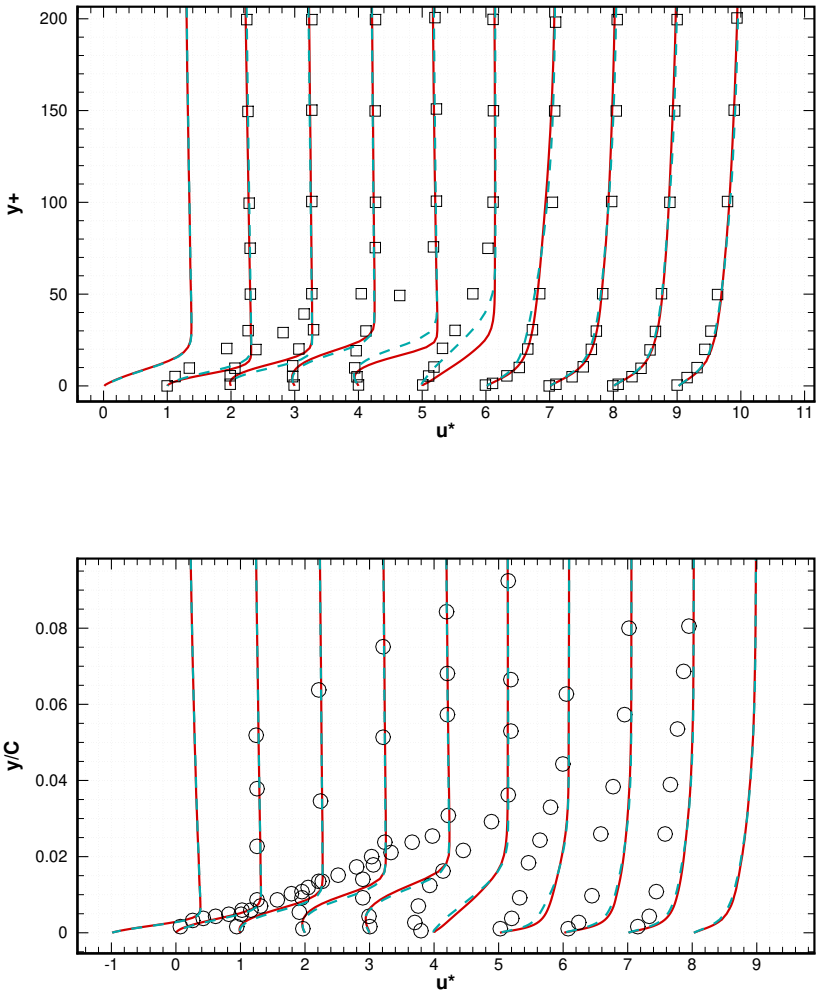

Fig. 9 Mean stream-wise velocity profiles compared with Smith [15] (left) and Shan et al [32] (right), from left to right are location at x/C=0.1, 0.2, 0.3, 0.4, 0.5, 0.6, 0.7, 0.8, 0.9, 1. The solid red line denotes iLES and the discontinued blue line denotes the LES.

surface. However, the disagreement is appeared at rest of the locations. The mean velocity profiles predicted by Shan et al [32] after location x=0.6 are not fully re-established, although resembling the turbulent velocity profile. This is partially due to the additional thin layer which has delayed re-attachment thus forming a longer separation zone that occupies half of the chord length, possibly giving not enough lengths for flow to re-establish [52]. It should also be noted that inflection points are observed, following Yang et al [57], inflection point is the necessary and sufficient condition for flow to be inviscidly unstable.

Figure 10 shows the enlarged view of separation zone, where mean stream-wise velocity profiles are gathered at one location. It can be seen that not only the thickness of the separation bubble is increasing towards the downstream direction, also does the amount of reversed flow. At each location, the amount of reversed flow has a small difference between current simulations and DNS, but major difference is found in the wall normal direction. For instance, at location x=0.5C, the reversed flow is about 6% of the free-stream velocity and located at y^+=5 for iLES, 6.5% at y^+=6 for LES and 6.1% at y^+=15 for DNS. Here, this difference seems to have little impact on the flow development at later stage, as the re-attached turbulent boundary layer is captured with excellent agreement. The maximum reversed flow of 12% is found at x=0.55C in current simulations (not being displayed in the figure and similar as in DNS of Smith [15]),

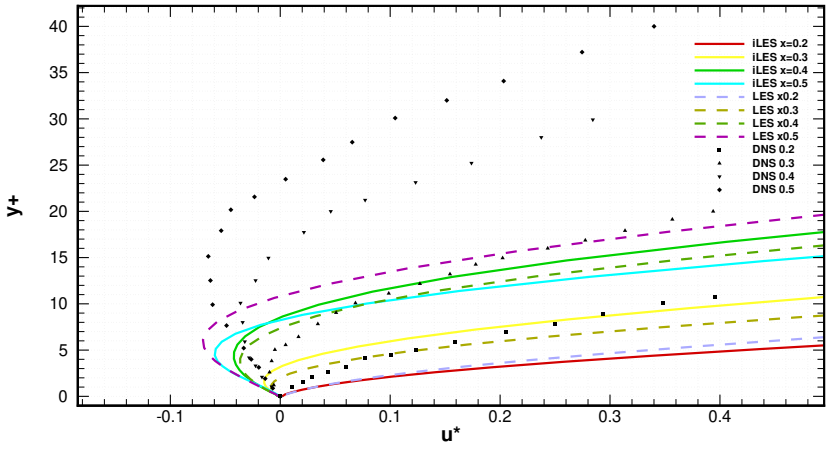

Fig. 10 Zoomed mean stream-wise velocity profiles at locations x/C=0.2, 0.3, 0.4, 0.5

while in DNS of Shan et al [32], 26% is found at x=0.6C. Alam and Sandham [58] concluded that velocity profiles with more than 15% of reversed flow are required for absolute stability (disturbances grow in time), while less than 15% are considered convective stability (disturbances grow in space). This condition is not met by current simulations. Hence it can be assumed that current separation bubble has similar behaviour to Alam [52] and Yang [57], where an inviscidly instability is triggered by Kelvin-Helmholtz mechanism.

The mean transverse and span-wise velocity profiles are displayed in Figure 11 and Figure 12 respectively. Similar patterns are captured by both iLES and LES approaches for mean transverse profiles, the main difference can be identified at locations x=0.5C, 0.6C and 0.7C, corresponding the re-attachment area. At the location near leading edge, the transverse velocity has been amplified to 350% of its free-stream magnitude then slowly been reduced until its lowest at location x=0.4C, right in the middle of the separation bubble. At locations closer to the re-attachment area, the transverse velocity has changed its direction fast towards the wall, then remains at about -110% after the re-attachment. The transverse profiles are quite similar to turbulent stream-wise profiles, but with an opposite direction. By examining the span-wise profiles in Figure 12, the flow is found dominated by two-dimensional motions at initial stage, as the mean span-wise velocity remains constant until x=0.5C, where a variation is observed, indicating the rise of three-dimensionality. The span-wise variation emerges firstly in viscous layer ($y^+ < 10$) then propagates upwards from the wall. At locations after x=0.5C, the profiles remain oscillated, highlighting the strong three-dimensional motion of the flow.

The root mean squared stream-wise and transverse fluctuations are plotted in Figure 13 and Figure 14. These quantities are strongly related to turbulence level of flow. At a short distance from the separation point, the flow is still laminar as no fluctuation appears in stream-wise and transverse directions. From location x=0.5C to x=0.6C, fluctuations are suddenly intensified near the wall, a transition to turbulence is believed to occur after the instability emerged in the separating boundary layer. The transition is also reflected by the strong gradient in plots of pressure coefficients 5 and skin friction coefficients 6. The stream-wise fluctuation peaks are at wall distance of $y^* \approx 7$ at x=0.6C for both iLES and LES approaches, but the former decreases much faster as distant away from the wall. Additionally, the transverse fluctuation peak is at $y^* \approx 15$ for iLES while for LES the peak is higher at $y^* \approx 30$. In other words, the iLES predicted a higher fluctuation in the near wall area at the re-attachment region (x≈0.6). The strongest fluctuation is found at around the transition-re-attachment area, similar as in Sato et al [59]. When the flow is re-established, both approaches predicted non-distinguishable fluctuation profiles. The R.M.S of kinetic energy is showed in Figure 15 and data of Smith [15] are also included. Apart from the re-attachment area (x=0.6C), the profiles are within satisfactory agreement with DNS reference, where flow remains smooth at first half of separation zone then being governed by strong turbulent activities from the re-attachment area until the tailing edge. It should be noted, the profile given by LES approach is closer to that of DNS reference than iLES at the re-attachment area, possibly suggesting an insufficient dissipation in the viscous layer for the latter approach.

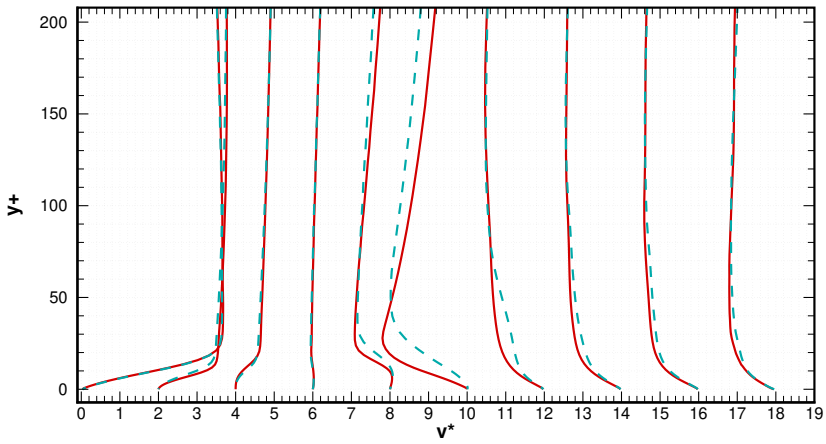

Fig. 11 Mean transverse velocity profiles, from left to right are location at x/C=0.1, 0.2, 0.3, 0.4, 0.5, 0.6, 0.7, 0.8, 0.9, 1. The solid red line denotes iLES and the discontinued blue line denotes the LES.

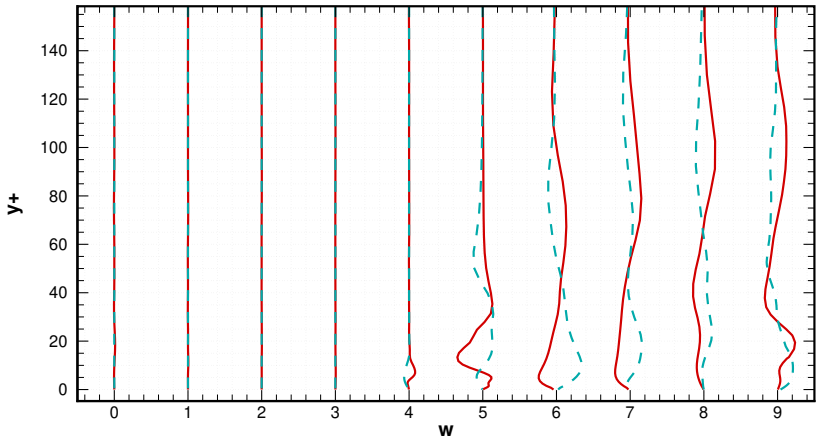

Fig. 12 Mean span-wise velocity profiles, from left to right are location at x/C=0.1, 0.2, 0.3, 0.4, 0.5, 0.6, 0.7, 0.8, 0.9, 1

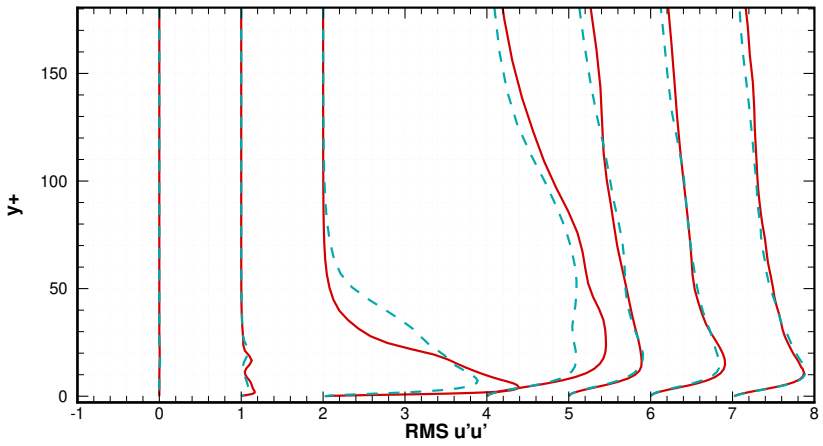

Fig. 13 Root mean square of stream-wise velocity fluctuation profiles, from left to right are location at x/C=0.4, 0.5, 0.6, 0.7, 0.8, 0.9, 1. The solid red line denotes iLES and the discontinued blue line denotes the LES.

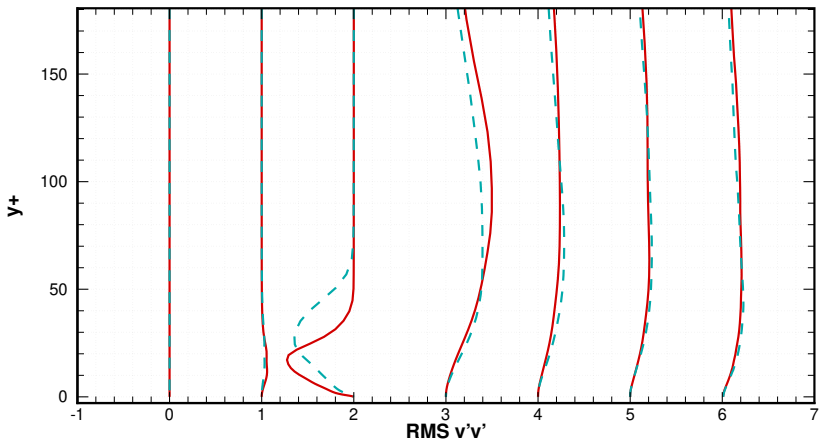

Fig. 14 Root mean square of transverse velocity fluctuation profiles, from left to right are location at x/C=0.4, 0.5, 0.6, 0.7, 0.8, 0.9, 1

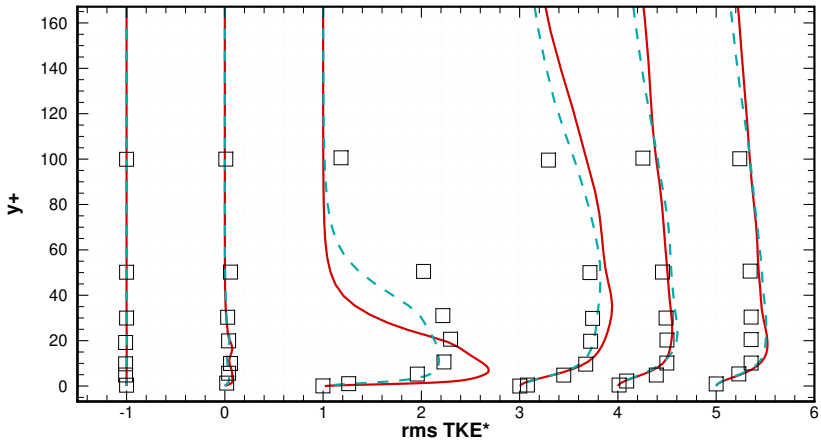

Fig. 15 Root mean square of TKE profiles compare with Smith[15], from left to right are location at x/C=0.4, 0.5, 0.6, 0.7, 0.8, 0.9

Finally, an overall physical phenomena can be summarised based on the time-averaged field as follows: The laminar boundary layer is formed after the flow past the leading edge of the aerofoil surface. Due to the adverse pressure gradient and curvature of the surface, the boundary layer separates at around x=0.23C. The separating boundary layer remains laminar for more than half of it's total length then undergoes transition to turbulent between x=0.5 to x=0.6, resulting a fast negative surge of skin friction coefficient and rapidly intensified turbulent fluctuations. The re-attachment takes place at around 0.6C, thus forming a separation bubble. The turbulent boundary layer is then established quickly and stays attached to the surface until finally sweeps off into the wake. Span-wise variation occurs before the transition to turbulence and its located about half of mean bubble length, the flow becomes three-dimensional then turbulent. The whole process shares similarities of Yang et al [57], where the flow past curvature induced plate. Currently, both iLES and LES have showed good reliability on time-averaged flow.

VI. Conclusion

The iLES and LES investigations have been carried out on the separated flow around NACA 0012 aerofoil, at incidence of 4 degrees and a moderate Reynolds number of 1×10^5. The total number of finite volume cells is kept as low as 7.7×10^6, which is 30% of the grid used in DNS of Smith [15] and much less than most of the LES in the literature. To validate the fidelity of the current numerical approach, results are compared with two DNS studies [15, 32] which were conducted under the same flow configurations.

The mean lift C_l and drag coefficients C_d are indistinguishable between iLES and LES, the variance is found within 10% compared to the experiment data from closest flow configuration. The mean surface pressure coefficients C_p are in excellent agreement with DNS of Smith [15], where the iLES gives a better prediction in the separated transitional region. The mean re-attachment is located at around x=0.6C for iLES and LES, in close agreement with Smith [15] who predicted x=0.56C and coincides with boundary layer transition region. The mean velocity profiles have showed a fully established turbulent boundary layer after the re-attachment, which are accurately matched with DNS of Smith [15]. However, it should be noted that in the separation zone, the current profiles are distinct to profiles of Smith [15] at a wall normal distance higher than y^+=10, although the amount of reversed flow is in satisfactory agreement. Further, at re-attachment location x=0.6C, the mean r.m.s of fluctuations predicted by LES have a better agreement to DNS than iLES.

The main findings and contributions of this paper are summarised as bellow: The current iLES approach based on 3rd order WENO scheme [26] is capable of dealing with wall bounded flow involving separation and transition. Although only a 2nd order overall accuracy is achieved, the computed mean quantities such as surface pressure coefficient, turbulent velocity profiles and turbulent kinetic energy profiles are in satisfactory agreement with DNS reference. Note

that despite the the current predicted near wall velocity profiles are different in the separation zone (Figure 9 and 10, hence a thinner separation bubble), the fully turbulent boundary layer at the re-attachment zone are still captured with excellent agreement. It has been proved that the near wall resolution is essential [60, 61] to accurately predict such complex flow. To overcome the current weakness, it is recommended to increase near wall resolution, by reducing the wall normal expansion ratio in the separation zone only. Also, the excessive turbulent kinetic energy is predicted by iLES at very near wall, indicating the possible lack of dissipation in the near wall region. It should also be pointed out a grid independence study is not conducted in current research due to a high computational cost, however it is still recommended when possible as it is an effective way to identify the numerical error from the grid. To author's knowledge, the current unstructured iLES approach embedded on OpenFOAM, is the first successful application on this non-canonical flow at moderate Reynolds number of 10^5.

Acknowledgments

This research has extensively employed the Cranfield University High Performance Computing (HPC) facility. The authors would like to acknowledge the support and guidance received from Dr Mick Knaggs at the Cranfield HPC department.

References

[1] Sakellariou, K., Rana, Z. A., and Jenkins, K. W., "Optimisation of the surfboard fin shape using computational fluid dynamics and genetic algorithms," *Proceedings of the Institution of Mechanical Engineers, Part P: Journal of Sports Engineering and Technology*, Vol. 231, No. 4, 2017, pp. 344–354. https://doi.org/10.1177/1754337117704538.

[2] Expósito, D., and Rana, Z. A., "Computational investigations into heat transfer over a double wedge in hypersonic flows," *Aerospace Science and Technology*, Vol. 92, 2019, pp. 839–846. https://doi.org/10.1016/j.ast.2019.07.013, URL https://doi.org/10.1016/j.ast.2019.07.013.

[3] BAGUL, P., RANA, Z. A., JENKINS, K. W., and KÖNÖZSY, L., "Computational engineering analysis of external geometrical modifications on MQ-1 unmanned combat aerial vehicle," *Chinese Journal of Aeronautics*, Vol. 33, No. 4, 2020, pp. 1154–1165. https://doi.org/10.1016/j.cja.2019.12.027.

[4] Rodi, W., "Comparison of LES and RANS calculations of the flow around bluff bodies," *Journal of Wind Engineering and Industrial Aerodynamics*, Vol. 69-71, 1997, pp. 55–75. https://doi.org/10.1016/S0167-6105(97)00147-5.

[5] Rumsey, C. L., and Nishino, T., "Numerical study comparing RANS and LES approaches on a circulation control airfoil," *International Journal of Heat and Fluid Flow*, Vol. 32, No. 5, 2011, pp. 847–864. https://doi.org/10.1016/j.ijheatfluidflow.2011.06.011.

[6] Li, Z., "DIGITAL WIND TUNNEL: AERODYNAMIC INVERSTIGATION OF A NACA 0012 AERFOIL COUPLING ANSYS ICEM AND OPENFOAM," Ph.D. thesis, Cranfield University, 2017.

[7] Zhang, Y., van Zuijlen, A., and van Bussel, G., "Massively separated turbulent flow simulation around non-rotating MEXICO blade by means of RANS and DDES approaches in OpenFOAM," *33rd AIAA Applied Aerodynamics Conference*, , No. June, 2015, pp. 1–10. https://doi.org/10.2514/6.2015-2716, URL http://arc.aiaa.org/doi/10.2514/6.2015-2716.

[8] Zhang, Y., Deng, S., and Wang, X., "RANS and DDES simulations of a horizontal-axis wind turbine under stalled flow condition using OpenFOAM," *Energy*, 2018. https://doi.org/10.1016/J.ENERGY.2018.11.014, URL https://www.sciencedirect.com/science/article/pii/S0360544218322187.

[9] Spalart, P. R., and Strelets, M. K., "Mechanisms of transition and heat transfer in a separation bubble," *Journal of Fluid Mechanics*, Vol. 403, 2000, pp. 329–349. https://doi.org/10.1017/S0022112099007077.

[10] Chapman, D., "Computational Aerodynamics Development and Outlook," *AIAA Journal*, Vol. 17, No. 12, 1979, pp. 1293–1313. https://doi.org/10.2514/6.1979-129.

[11] Choi, H., and Moin, P., "Grid-point requirements for large eddy simulation: Chapman's estimates revisited," *Physics of Fluids*, Vol. 24, No. 1, 2012. https://doi.org/10.1063/1.3676783.

[12] Drikakis, D., Fureby, C., Grinstein, F. F., and Youngs, D., "Simulation of transition and turbulence decay in the Taylor-Green vortex," *Journal of Turbulence*, Vol. 8, 2007, pp. 1–12. https://doi.org/10.1080/14685240701250289.

[13] Grinstein, F. F., Margolin, L. G., and Rider, W. J., *Implicit Large Eddy Simulation: computing turbulent fluid dynamics*, Cambridge University Press, 2007.

[14] Davidson, L., Cokljat, D., Frohlich, J., Leschziner, M. A., Mellen, C., and Rodi, W., *LESFOIL: Large Eddy Simulation of Flow Around a High Lift Airfoil*, 2003. https://doi.org/10.1007/978-3-540-89956-3_9, URL http://www.springerlink.com/index/10.1007/978-3-540-89956-3_9.

[15] Smith, T. A., and Ventikos, Y., "Boundary layer transition over a foil using direct numerical simulation and large eddy simulation," *Physics of Fluids*, Vol. 31, No. 12, 2019. https://doi.org/10.1063/1.5126663, URL https://doi.org/10.1063/1.5126663.

[16] Boris, J. P., "On large eddy simulation using subgrid turbulence models Comment," *Whither Turbulence ? or Turbulence at the Crossroads*, 1990, pp. 344–353. https://doi.org/10.1007/3-540-52535-1_53.

[17] Beaudan, P., and Moin, P., "Numerical experiments on the flow past a circular cylinder at sub-critical Reynolds number," *Stanford University*, , No. Report No. TF-62, 1994, pp. 1–262.

[18] Ouvrard, H., Koobus, B., Dervieux, A., and Salvetti, M. V., "Classical and variational multiscale LES of the flow around a circular cylinder on unstructured grids," *Computers and Fluids*, Vol. 39, No. 7, 2010, pp. 1083–1094. https://doi.org/10.1016/j.compfluid.2010.01.017, URL http://dx.doi.org/10.1016/j.compfluid.2010.01.017.

[19] Drikakis, D., and Rider, W., *High-Resolution Methods for Incompressible and Low-Speed Flows*, 2005. https://doi.org/10.1007/b137615.

[20] Liu, X. D., Osher, S., and Chan, T., "Weighted Essentially Non-Oscillatory Schemes," *Journal of Computational Physics*, 1994, pp. 200–212.

[21] Hahn, M., "Implicit Large-Eddy Simulation of Low-Speed Separated Flows Using High-Resolution Methods," Ph.D. thesis, 2008.

[22] Dumbser, M., and Käser, M., "Arbitrary high order non-oscillatory finite volume schemes on unstructured meshes for linear hyperbolic systems," *Journal of Computational Physics*, Vol. 221, No. 2, 2007, pp. 693–723. https://doi.org/10.1016/j.jcp.2006.06.043.

[23] Tsoutsanis, P., Titarev, V. A., and Drikakis, D., "WENO schemes on arbitrary mixed-element unstructured meshes in three space dimensions," *Journal of Computational Physics*, Vol. 230, No. 4, 2011, pp. 1585–1601. https://doi.org/10.1016/j.jcp.2010.11.023, URL http://dx.doi.org/10.1016/j.jcp.2010.11.023.

[24] Tsoutsanis, P., Antoniadis, A. F., and Drikakis, D., "WENO schemes on arbitrary unstructured meshes for laminar, transitional and turbulent flows," *Journal of Computational Physics*, Vol. 256, 2014, pp. 254–276. https://doi.org/10.1016/j.jcp.2013.09.002, URL http://dx.doi.org/10.1016/j.jcp.2013.09.002.

[25] Zeng, K., Li, Z., Rana, Z. A., and Jenkins, K. W., "Implicit Large Eddy Simulations of Turbulent Flow around a Square Cylinder at Re = 22,000," *Computers Fluids*, Vol. 226, 2021, p. 105000. https://doi.org/10.1016/j.compfluid.2021.105000, URL https://doi.org/10.1016/j.compfluid.2021.105000.

[26] Martin, T., and Shevchuk, I., "Implementation and Validation of Semi-Implicit WENO Schemes Using OpenFOAM®," *Computation*, Vol. 6, No. 1, 2018, p. 6. https://doi.org/10.3390/computation6010006.

[27] Lissaman, P. B. S., "Low-reynolds-number airfoils," *Annual Review of Fluid Mechanics*, 1983, pp. 223–239.

[28] Jones, L. E., Sandberg, R. D., and Sandham, N. D., "Direct numerical simulations of forced and unforced separation bubbles on an airfoil at incidence," *Journal of Fluid Mechanics*, Vol. 602, 2008, pp. 175–207. https://doi.org/10.1017/S0022112008000864.

[29] Bertolotti, F. . P., Herbert, T., and Spalart, P. R., "Linear and nonlinear stability of the blasius boundary layer," *Journal of Fluid Mechanics*, Vol. 242, No. 34, 1992, pp. 441–474. https://doi.org/10.1017/S0022112092002453.

[30] Herbert, T., "Parabolized stability equations," *Annual Review of Fluid Mechanics*, Vol. 29, 1997, pp. 245–283. https://doi.org/10.1146/annurev.fluid.29.1.245.

[31] Rodríguez, I., Lehmkuhl, O., Borrell, R., and Oliva, A., "Direct numerical simulation of a NACA0012 in full stall," *International Journal of Heat and Fluid Flow*, Vol. 43, 2013, pp. 194–203. https://doi.org/10.1016/j.ijheatfluidflow.2013.05.002, URL http://dx.doi.org/10.1016/j.ijheatfluidflow.2013.05.002.

[32] Shan, H., Jiang, L., and Liu, C., "Direct numerical simulation of flow separation around a NACA 0012 airfoil," *Computers and Fluids*, Vol. 34, No. 9, 2005, pp. 1096–1114. https://doi.org/10.1016/j.compfluid.2004.09.003.

[33] Mellen, C. P., Fröhlich, J., and Rodi, W., "Lessons from the European LESFOIL project on LES of flow around an airfoil," *40th AIAA Aerospace Sciences Meeting and Exhibit*, , No. c, 2002. https://doi.org/10.2514/6.2002-111.

[34] NICOUD, F., and DUCROS, F., "Subgrid-Scale Stress Modelling Based on the Square of the Velocity Gradient Tensor," *Flow, Turbulence and Combustion*, Vol. 62, 1999, pp. 183–200. https://doi.org/10.1016/j.jcp.2004.10.018.

[35] Moukalled, F., Mangani, L., and Darwish, M., *The Finite Volume Method in Computational Fluid Dynamics*, Vol. 113, 2016. https://doi.org/10.1007/978-3-319-16874-6, URL http://www.scopus.com/inward/record.url?eid=2-s2.0-84939129919&partnerID=tZOtx3y1.

[36] Jasak, H., "Error Analysis and Estimation for the finite volume method with applications to fluid flows," Ph.D. thesis, 1996.

[37] Warming, R. F., and Beam, R. M., "Upwind second-order difference schemes and applications in aerodynamic flows," *AIAA Journal*, Vol. 14, No. 9, 1976, pp. 1241–1249. https://doi.org/10.2514/3.61457.

[38] Cao, Y., and Tamura, T., "Large-eddy simulations of flow past a square cylinder using structured and unstructured grids," *Computers and Fluids*, Vol. 137, 2016, pp. 36–54. https://doi.org/10.1016/j.compfluid.2016.07.013, URL http://dx.doi.org/10.1016/j.compfluid.2016.07.013.

[39] Khosla, P. K., and Rubin, S. G., "A diagonally dominant second-order accurate implicit scheme," *Computers and Fluids*, Vol. 2, No. 2, 1974, pp. 207–209. https://doi.org/10.1016/0045-7930(74)90014-0.

[40] Pringuey, T., and Cant, R. S., "High order schemes on three-dimensional general polyhedral meshes - Application to the level set method," *Communications in Computational Physics*, Vol. 12, No. 1, 2012, pp. 1–41. https://doi.org/10.4208/cicp.260511.050811a.

[41] Shu, C.-w., "Essentially non-oscillatory and weighted essentially non-oscillatory schemes for hyperbolic conservation laws," *ICASE Report*, 97-65, 1998, pp. 325–432. https://doi.org/10.1007/BFb0096355, URL http://link.springer.com/10.1007/BFb0096355.

[42] Ollivier-Gooch, C., and Van Altena, M., "A high-order-accurate unstructured mesh finite-volume scheme for the advection-diffusion equation," *Journal of Computational Physics*, Vol. 181, No. 2, 2002, pp. 729–752. https://doi.org/10.1006/jcph.2002.7159.

[43] Gärtner, J. W., Kronenburg, A., and Martin, T., "Efficient WENO library for OpenFOAM," *SoftwareX*, Vol. 12, 2020, p. 100611. https://doi.org/10.1016/j.softx.2020.100611, URL https://doi.org/10.1016/j.softx.2020.100611.

[44] Tian, G., and Xiao, Z., "New insight on large-eddy simulation of flow past a circular cylinder at subcritical Reynolds number 3900," *AIP Advances*, Vol. 10, No. 8, 2020. https://doi.org/10.1063/5.0012358, URL https://doi.org/10.1063/5.0012358.

[45] Asada, K., and Kawai, S., "Large-eddy simulation of airfoil flow near stall condition at Reynolds number 2.1 × 10 ⁶," *Physics of Fluids*, Vol. 30, No. 8, 2018, p. 085103. https://doi.org/10.1063/1.5037278, URL http://aip.scitation.org/doi/10.1063/1.5037278.

[46] Castiglioni, G., and Domaradzki, J. A., "A numerical dissipation rate and viscosity in flow simulations with realistic geometry using low-order compressible Navier-Stokes solvers," *Computers and Fluids*, Vol. 119, 2015, pp. 37–46. https://doi.org/10.1016/j.compfluid.2015.07.004, URL http://dx.doi.org/10.1016/j.compfluid.2015.07.004.

[47] Zhang, W., and Samtaney, R., "Assessment of spanwise domain size effect on the transitional flow past an airfoil," *Computers and Fluids*, Vol. 124, 2016, pp. 39–53. https://doi.org/10.1016/j.compfluid.2015.10.008, URL http://dx.doi.org/10.1016/j.compfluid.2015.10.008.

[48] Fröhlich, J., Mellen, C. P., Rodi, W., Temmerman, L., and Leschziner, M. A., "Highly resolved large-eddy simulation of separated flow in a channel with streamwise periodic constrictions," *Journal of Fluid Mechanics*, Vol. 526, 2005, pp. 19–66. https://doi.org/10.1017/S0022112004002812.

[49] Piomelli, U., and Balaras, E., "WALL-LAYER MODELS FOR LARGE-EDDY SIMULATIONS," *Annual Review of Fluid Mechanics*, Vol. 34, 2002, pp. 349–374.

[50] Piomelli, U., "Wall-layer models for large-eddy simulations," *Progress in Aerospace Sciences*, Vol. 44, No. 6, 2008, pp. 437–446. https://doi.org/10.1016/j.paerosci.2008.06.001.

[51] Sheldahl, R. E., and Klimas, P. C., "Aerodynamic characteristics of seven symmetrical airfoil sections through 180-degree angle of attack for use in aerodynamic analysis of vertical axis wind turbines." Tech. rep., 1981.

[52] Alam, M., and Sandham, N. D., "Direct numerical simulation of 'short' laminar separation bubbles with turbulent reattachment," *Journal of Fluid Mechanics*, Vol. 403, 2000, pp. 223–250. https://doi.org/10.1017/S0022112099007119.

[53] Lehmkuhl, O., Rodríguez, I., Baez, A., Oliva, A., and Pérez-Segarra, C. D., "On the large-eddy simulations for the flow around aerodynamic profiles using unstructured grids," *Computers and Fluids*, Vol. 84, 2013, pp. 176–189. https://doi.org/10.1016/j.compfluid.2013.06.002, URL http://dx.doi.org/10.1016/j.compfluid.2013.06.002.

[54] Kojima, R., Nonomura, T., Oyama, A., and Fujii, K., "Large-Eddy Simulation of Low-Reynolds-Number Flow Over Thick and Thin NACA Airfoils," *Journal of Aircraft*, Vol. 50, No. 1, 2013, pp. 187–196. https://doi.org/10.2514/1.C031849, URL http://arc.aiaa.org/doi/10.2514/1.C031849.

[55] Lee, D., Kawai, S., Nonomura, T., Anyoji, M., Aono, H., Oyama, A., Asai, K., and Fujii, K., "Mechanisms of surface pressure distribution within a laminar separation bubble at different Reynolds numbers," *Physics of Fluids*, Vol. 27, No. 2, 2015. https://doi.org/10.1063/1.4913500.

[56] Thomareisa, N., and Papadakis, G., "Effect of trailing edge shape on the separated flow characteristics around an airfoil at low reynolds number: A numerical study," *Physics of Fluids*, Vol. 29, No. 1, 2017. https://doi.org/10.1063/1.4973811.

[57] Yang, Z., and Voke, P. R., "Large-eddy simulation of boundary-layer separation and transition at a change of surface curvature," *Journal of Fluid Mechanics*, Vol. 439, 2001, pp. 305–333.

[58] Alam, M., and Sandham, N. D., "Direct numerical simulation of 'short' laminar separation bubbles with turbulent reattachment," *Journal of Fluid Mechanics*, Vol. 410, 2000, pp. 1–28. https://doi.org/10.1017/S0022112099008976.

[59] Sato, M., Asada, K., Nonomura, T., Kawai, S., and Fujii, K., "Large-Eddy Simulation of NACA 0015 Airfoil Flow at Reynolds Number of 1.6×106," *AIAA Journal*, Vol. 55, No. 2, 2017, pp. 673–679. https://doi.org/10.2514/1.J054963, URL http://arc.aiaa.org/doi/10.2514/1.J054963.

[60] Morgan, P. E., and Visbal, M. R., "Large-eddy simulation modeling issues for flow around wing sections," *33rd AIAA Fluid Dynamics Conference and Exhibit*, , No. June, 2003, pp. 1–17. https://doi.org/10.2514/6.2003-4152.

[61] Hahn, M., and Drikakis, D., "Implicit large-eddy simulation of swept-wing flow using high-resolution methods," *AIAA Journal*, Vol. 47, No. 3, 2009, pp. 618–630. https://doi.org/10.2514/1.37806.

Implicit large eddy simulation of the flow past NACA0012 aerofoil at a Reynolds number of 1x10^5

Li, Zhuoneng

2024-01-04

Li Z, Rana ZA. (2024) Implicit large eddy simulation of the flow past NACA0012 aerofoil at a Reynolds number of 1x10^ 5. In AIAA SCITECH 2024 Forum, 8-12 January 2024, Orlando, FL, USA, Paper Number 2024-2682

https://doi.org/10.2514/6.2024-2682